Implementation of Pairwise Longitudinal Coupling in a Three-Qubit Superconducting Circuit

Tanay Roy, Suman Kundu, Madhavi Chand, Sumeru Hazra, N. Nehra,[†] R. Cosmic,[‡] A. Ranadive,
Meghan P. Patankar, Kedar Damle, and R. Vijay[*]

*Department of Condensed Matter Physics and Materials Science, Tata Institute of Fundamental Research,
Homi Bhabha Road, Mumbai 400005, India*
*Department of Theoretical Physics, Tata Institute of Fundamental Research,
Homi Bhabha Road, Mumbai 400005, India*

We present the "trimon," a multimode superconducting circuit implementing three qubits with all-to-all longitudinal coupling. This always-on interaction enables simple implementation of generalized controlled-NOT gates which form a universal set. Furthermore, two of the three qubits are protected against Purcell decay while retaining measurability. We demonstrate high-fidelity state swapping operations between two qubits and characterize the coupling of all three qubits to a neighboring transmon qubit. Our results offer a different paradigm for multiqubit architecture with applications in quantum error correction, quantum simulations, and quantum annealing.

I. INTRODUCTION

Controlling and manipulating the interactions between multiple qubits is at the heart of quantum-information processing, and the superconducting-circuit architecture [1] has emerged as a leading candidate. Previous demonstrations of multiqubit devices [2–8] have used transmon qubits [9] along with separate coupling elements to implement transverse interqubit coupling. Typically, this transverse coupling is weak and restricted to nearest neighbors, which limits the kind of multiqubit operations that can be performed. While the idea of longitudinal interqubit coupling [10,11] has existed for more than a decade, there has been renewed interest in it recently, with proposals for universal quantum computing [12–15] and quantum annealing [16] based on modern high-coherence qubits like the transmon. The transmon design uses the lowest two levels of a single anharmonic oscillator mode to implement a qubit. Extending this idea to a circuit that supports several oscillator modes, one can implement a multiqubit system with strong longitudinal coupling [17,18]. Previous experiments have shown evidence of longitudinal coupling [19,20] but have not demonstrated multiqubit operations, and their coherence times have not matched those of modern transmon qubits.

[*]Corresponding author.
r.vijay@tifr.res.in
[†]Present address: Department of Physics, University of Wisconsin–Madison, Madison, WI 53706, USA.
[‡]Present address: Research Center for Advanced Science and Technology (RCAST), The University of Tokyo, Meguro-ku, Tokyo 153-8904, Japan.

In this article, we present the "trimon," a quantum device implementing a three-qubit system that arises from a single superconducting circuit. Our device [Fig. 1(a)] is based on the Josephson ring modulator (JRM) consisting of four nominally identical Josephson junctions in a superconducting loop to implement three orthogonal electrical modes [21]. This three-mode structure has previously been exploited to couple different harmonic oscillators for parametric amplification [22], while, more recently, it has been proposed as a coupling element between two qubits [16]. Here, we capacitively shunt the JRM by connecting superconducting pads to each node [Fig. 1(b)] to create three coupled anharmonic oscillator modes: two dipolar and one quadrupolar [Fig. 1(c)]. Each mode has properties similar to 3D transmon qubits [23], with the resonant frequency and anharmonicity controllable by design. The longitudinal interqubit coupling [16] of the cross-Kerr type originates due to the sharing of the four junctions amongst all three modes. One of the two dipolar modes couples directly to the host 3D electromagnetic cavity [Fig. 1(c)]; we call this dipolar mode the A qubit. The other dipolar mode (qubit B) and the quadrupolar mode (qubit C) ideally stay uncoupled from the cavity and hence are protected from Purcell decay [17]. However, this protection does not preclude cavity-based measurement of qubits B and C; the interqubit longitudinal coupling results in dispersive shifts similar to that of qubit A (Appendix A).

II. DEVICE DESIGN AND PROPERTIES

The Hamiltonian of our circuit (Appendix A) when operated at zero flux in the loop is given by
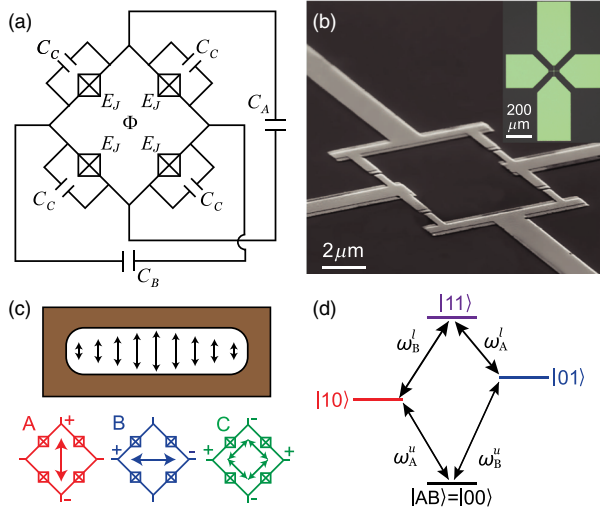
FIG. 1. (a) Circuit schematic and (b) scanning-electron-microscope image of the trimon device. (Inset) Optical image (false color) of the full device. The two pairs of capacitor pads have different sizes to obtain different transition frequencies for qubits A and B. (c) The device is placed at the center of a rectangular copper cavity with qubit A's dipole (the red arrow) aligned to the cavity's electric field in the TE_{101} mode (the black arrows). Qubit B's orthogonal dipole (the blue arrow) and qubit C's quadrupole (the green arrows) are also indicated. (d) Energy level diagram of the coupled two-qubit subspace of A and B, with qubit C in its ground state. The $\sigma_z\sigma_z$ coupling makes the transition frequency of each qubit dependent on the state of the other. The upper ($\omega_{A,B}^u$) and lower ($\omega_{A,B}^l = \omega_{A,B}^u - 2J_{AB}$) band transition frequencies for each qubit are indicated.

$$\frac{1}{\hbar}H_{system} = -\frac{1}{2}\left[\sum_{i=A,B,C}(\omega_i - 2\beta_i)\sigma_z^i + \sum_{i\neq j}J_{ij}\sigma_z^i\sigma_z^j\right]$$
$$+ \left(\omega_{cav} - \sum_{i=A,B,C}\chi_i\sigma_z^i\right)a^\dagger a, \qquad (1)$$

where $\omega_{i=A,B,C}$ are uncoupled qubit transition frequencies, $\beta_i = J_i + J_{ij} + J_{ki}, i \neq j \neq k$ are the shifts due to self-Kerr (J_i) and cross-Kerr (J_{ij}) terms, $\chi_{i=A,B,C}$ are the dispersive shifts and $\omega_{cav} - \sum_i \chi_i$ is the cavity frequency, with all qubits in the ground state. While the transition frequencies can be tuned with a nonzero flux, it will introduce additional terms in the Hamiltonian (Appendix A), and here we focus on the zero-flux case. Because of the longitudinal $\sigma_z\sigma_z$ coupling, each qubit now has four possible values of transition frequency that depend on the state of the other two qubits. For simplicity, the level diagram shown in Fig. 1(d) is restricted to the two-qubit subspace spanned by qubits A and B (with qubit C frozen in its ground state) but reveals all of the important features. For a given qubit, we label the transition frequency to be in the upper (ω_i^u) or lower ($\omega_i^l = \omega_i^u - 2J_{AB}$) band when the partner qubit is in the ground or excited state, respectively. A rotation on qubit A conditioned on the state of qubit B can be realized by a microwave tone at frequency ω_A^l (B in the excited state) or ω_A^u (B in the ground

state). A single pulse at ω_A^l with the appropriate amplitude and length then implements a conventional controlled-NOT (CNOT) gate [24,25] up to a $-90°$ phase, which we call a $-i$CNOT$_{BA}$ gate. This extra phase can be accounted for in this architecture by simply shifting the rotation axis of all subsequent pulses on qubit B (Appendix B).

While the always-on $\sigma_z\sigma_z$ coupling leads to simple two-qubit gates, single-qubit gates become less trivial. In order to perform a single-qubit rotation on B independent of the state of A, one now needs to apply pulses at both ω_B^l and ω_B^u. This approach is similar to an NMR technique [26], where a single broadband pulse covering both frequencies is used. We use a multifrequency pulse instead due to the large ($J_{AB}/\pi = 201.2$ MHz) coupling in our system. Doing so also automatically accounts for the phase evolution in the qubit states due to the always-on $\sigma_z\sigma_z$ coupling [26]. In general, for such an N-qubit system, pulses at 2^{N-1} different frequencies will be required to perform a single-qubit gate, 2^{N-2} frequencies for two-qubit gates, and so on. However, for $N = 3$, the frequency crowding is manageable and the multifrequency pulses can be generated using sideband modulation of a single microwave source (Appendix B).

The trimon devices are fabricated on a high-resistivity intrinsic silicon chip using standard electron-beam lithography and double-angle evaporation of aluminium. The device, placed inside a two-port copper cavity with asymmetric coupling is put inside light-tight radiation and cryoperm shields and cooled to 30 mK in a cryogen-free dilution refrigerator. The first-stage amplification of the output signal is done by a near-quantum-limited lumped-element Josephson parametric amplifier (LJPA) [27]. Details of the measurement setup are provided in Appendix B. The resonant frequency and linewidth of our measurement cavity (bare) are measured to be $\omega_{bare}/2\pi = 7.23$ GHz and $\kappa/2\pi = 3.9$ MHz, respectively. The upper- and lower-band transition frequencies are extracted using Ramsey-fringe experiments.

III. EXPERIMENTAL RESULTS

The results of spectroscopy and coherence measurements on all three qubits are tabulated in Table I, indicating coherence properties comparable to typical 3D transmon qubits [5]. Note that the anharmonicities (α) are about a factor of 2 smaller than the typical transmon values, but they can be increased by adjusting the design parameters. The interqubit coupling (J_{ij}) numbers confirm the strong, pairwise longitudinal coupling. We obtain the best relaxation time (T_1) for qubit B as it is decoupled from the cavity. The $T_{1,B} \sim 50 \mu$s is consistent with our measurements on regular transmon qubits when they are detuned sufficiently from the cavity so that the relaxation time is not limited by Purcell decay. While we expect the T_1 for qubit C to be similar to that of B, we observe it to be smaller. This trend is seen across several devices, and one possible reason could be the unavoidable spread in the Josephson

TABLE I.   Parameters and coherence properties of the trimon. The transition frequency (ω^u) of each qubit with the other two qubits in their ground state is listed along with the anharmonicity (α), the relaxation time (T_1), the Hahn-echo time (T_2^E), the dispersive shift (χ), and the interqubit coupling strength (J_{ij}).

Qubit	$\omega^u/2\pi$ (GHz)	$\alpha/2\pi$ (MHz)	T_1 (μs)	T_2^E (μs)	$\chi/2\pi$ (MHz)	J_{ij}/π (MHz)
A	5.5585	−111.0	20.6	39.7	−0.332	$J_{AB}/\pi = 201.2$
B	6.1470	−116.0	51.4	64.8	−0.376	$J_{BC}/\pi = 253.0$
C	7.0180	−138.6	26.2	32.3[a]	−0.386	$J_{CA}/\pi = 232.0$

[a]For qubit C, the Ramsey-fringe decay time (T_2^R) is indicated, as we were unable to get a clear Hahn-echo signal (Appendix C).

energies of the four junctions. As a result, qubits B and C develop a small dipolar component along the cavity field leading to a finite qubit-cavity coupling (Appendix C). Since qubit C ($\omega_C^u/2\pi = 7.0180$ GHz) is much closer to the bare-cavity frequency ($\omega_{\text{bare}}/2\pi = 7.23$ GHz) than qubit B ($\omega_B^u/2\pi = 6.1470$ GHz), even a small coupling to the cavity can reduce the T_1 due to Purcell decay. Further investigation is planned to understand this effect.

We first demonstrate our single-pulse CNOT gate by preparing a Bell state using qubits A and B. For all experiments, we start by performing a strong measurement and process only those data for which this measurement yields the state $|000\rangle$. This operation initializes the trimon in the $|000\rangle$ state with 99.7% probability. Since qubit B is now initialized in the ground state, a $\pi/2$ pulse at frequency ω_B^u is sufficient to prepare the state $|0\rangle(|0\rangle + |1\rangle)/\sqrt{2}$. Finally, the CNOT$_{BA}$ gate is implemented by a π pulse at ω_A^l to prepare the two-qubit Bell state $(|00\rangle + |11\rangle)/\sqrt{2}$. Note

that the π pulse at ω_A^l implements a native $-i$CNOT$_{BA}$ gate, and we shift the phase of all subsequent pulses of the control qubit (B) by 90° to construct the conventional CNOT gate. The real and imaginary parts of the reconstructed density matrix along with the pulse sequence are shown in Fig. 2. The fidelity of the Bell state is found to be 0.974 ± 0.003 using two-qubit tomography and maximum-likelihood estimation (MLE) and does not account for finite
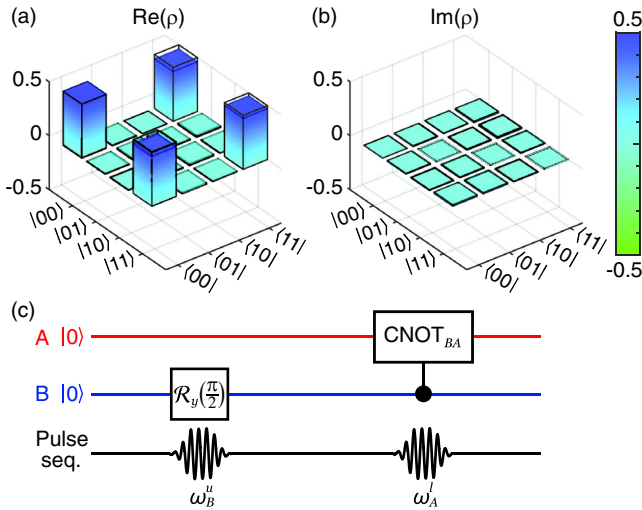

FIG. 2. (a),(b) Real and imaginary parts of the reconstructed density matrix (MLE) for the Bell state $(|00\rangle + |11\rangle)/\sqrt{2}$, which we prepare using the single-pulse CNOT gate. Here, the filled colored bars are experimental data, while transparent bars with black boundaries denote ideal values corresponding to the intended state. (c) The quantum circuit for preparing the Bell state and the corresponding pulse sequence with transition frequencies are indicated. The $\pi/2$-pulse length at ω_B^u is 281 ns, while the π-pulse (CNOT$_{BA}$) length at ω_A^l is 241 ns.
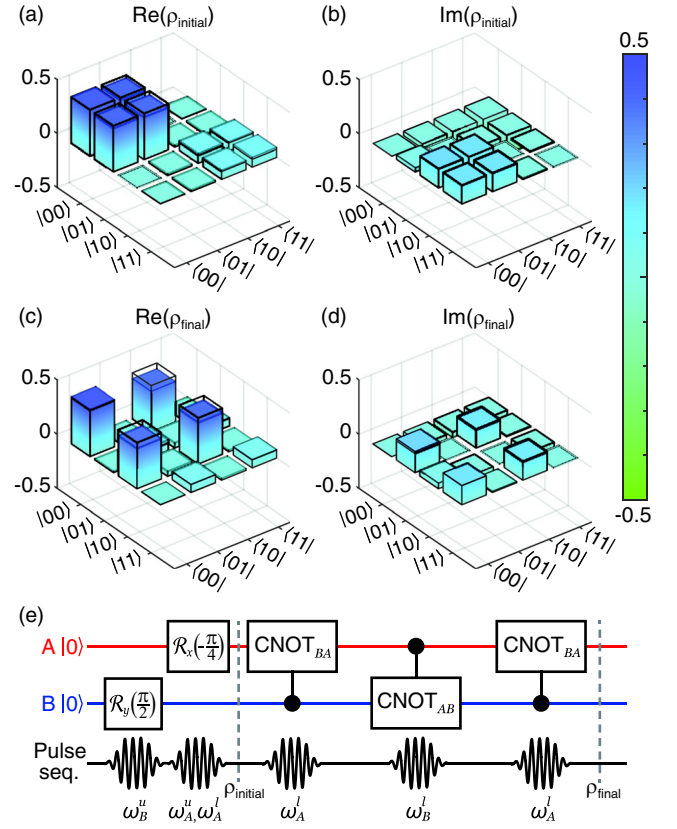
FIG. 3. Real and imaginary parts of reconstructed density matrices (a),(b) before SWAP operation and (c),(d) after SWAP operation. The filled colored bars are the experimental data, while transparent bars with black boundaries denote ideal values corresponding to the intended state. (e) The quantum circuit and the corresponding pulse sequence with transition frequencies are indicated. The $\pi/2$-pulse length at ω_B^u is 281 ns, the $\pi/4$-pulse length at ω_A^u and ω_A^l is 108 ns, and the π-pulse lengths at ω_A^l and ω_B^l are 241 and 497 ns, respectively.
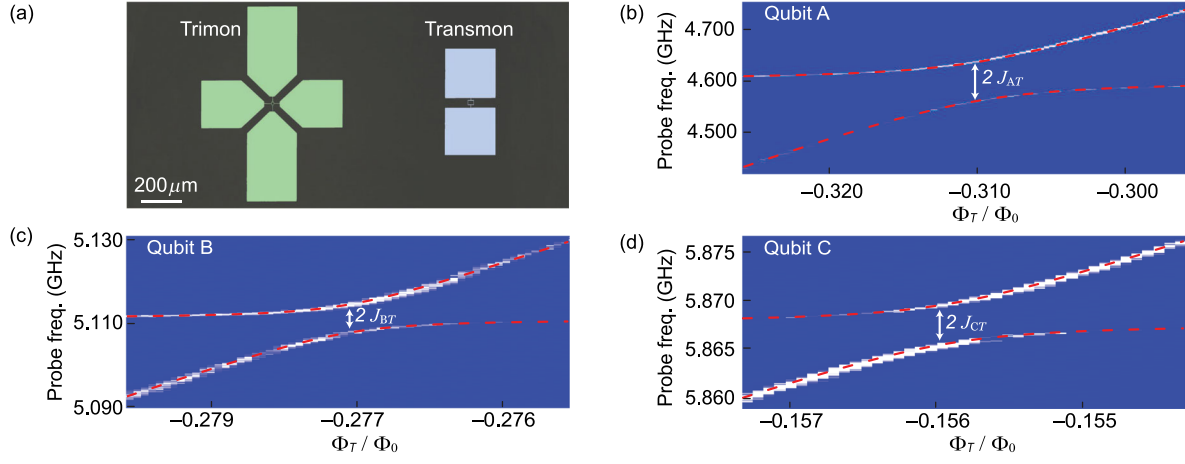
FIG. 4. (a) False-colored optical image of the device showing a trimon and a transmon with a spacing of about 1 mm. The dipole of the transmon is aligned with that of qubit A of the trimon device. (b)–(d) Avoided crossing of the transmon qubit's transition with qubits A, B, and C. Φ_T is the flux in the transmon's loop area and Φ_0 is the magnetic flux quantum. The dashed red lines are a fit to the location of the transition frequencies using the universal avoided crossing formula. We extract the couplings $J_{AT}/\pi = 77.6$ MHz, $J_{BT}/\pi = 6.8$ MHz, and $J_{CT}/\pi = 3.8$ MHz for the three qubits, respectively.

measurement fidelity (Appendix F). The uncertainty quoted is the standard deviation in the fidelity in successive data sets, while the uncertainty obtained from bootstrapping is about an order of magnitude lower. We prepared various other Bell states and obtained similar fidelities.

Taking the idea further, we demonstrate an optimal SWAP gate [28,29], for the first time in circuit-QED architecture, which swaps the quantum states of two qubits. Our SWAP gate is realized by three CNOT pulses on qubits A and B: $\text{SWAP}_{AB} = \text{CNOT}_{BA}\text{CNOT}_{AB}\text{CNOT}_{BA}$. We prepare the initial state $|i\rangle = [\cos(\pi/8)|0\rangle + i\sin(\pi/8)|1\rangle]_A \otimes [(|0\rangle + |1\rangle)/\sqrt{2}]_B$ with the fidelity 0.983 ± 0.005 and then, using our SWAP gate, generate the final state $|f\rangle = [(|0\rangle + |1\rangle)/\sqrt{2}]_A \otimes [\cos(\pi/8)|0\rangle + i\sin(\pi/8)|1\rangle]_B$, with the fidelity 0.971 ± 0.005. The reconstructed density matrices of the initial and final two-qubit states are shown in Fig. 3. If qubit B is initially in the ground state, the SWAP gate can be simplified to a transfer gate which moves a quantum state from A to B and requires only two CNOT gates. We transfer the state $(|0\rangle + |1\rangle)/\sqrt{2}$ from qubit A to B and obtain a final-state fidelity of 0.973 ± 0.005 (Appendix G). In order to estimate single-qubit-gate (consisting of two pulses at upper- and lower-band frequencies) fidelities, we perform randomized benchmarking [30] and obtain mean gate fidelities of 0.9928 ± 0.0001 and 0.9858 ± 0.0002 for qubits A and B, respectively (Appendix E). Further improvements in fidelity are possible by optimizing the qubit-cavity coupling and reducing pulse lengths. Given the qubit anharmonicities (Table I), we can easily reduce the pulse lengths (see the captions of Figs. 2 and 3) by a factor of 10 without any risk of leakage out of the computational subspace. The pulse lengths in this experiment are restricted due to the limited microwave power available in our setup and the relatively weak coupling of qubits to the cavity (Appendix C).

Since qubits A and B have nearly orthogonal dipole moments, their coupling to a nearby qubit, say a transmon, depends strongly on whether the transmon's dipole is aligned [31] to qubit A or B. To characterize the dipolar coupling between the trimon and a transmon qubit, we fabricate both the devices with their centers 1 mm apart on the same chip, as shown in Fig. 4(a). The loop area of the transmon is about 7 times larger than that of the trimon. This difference in area allows us to tune the transition frequency of the transmon while keeping the transition frequencies of qubits A, B, and C relatively unchanged. Spectroscopic data in Figs. 4(b)–4(d) show strong coupling ($J_{AT}/\pi = 77.6$ MHz) between the transmon and qubit A since their dipoles are aligned, whereas qubit B ($J_{BT}/\pi = 6.8$ MHz) and qubit C ($J_{CT}/\pi = 3.8$ MHz) show much weaker coupling, as expected. Using electromagnetic simulations, we verify that the finite coupling of qubits B and C is consistent with a 10%–20% variability in the Josephson energies of the JRM arising due to fabrication uncertainties. The variable dipolar coupling of the three qubits to the transmon qubit nearby confirms the symmetry of the three qubit modes and can be used to estimate the extent to which qubits B and C are protected against Purcell decay (Appendix C).

IV. DISCUSSION AND CONCLUSIONS

We now discuss the possibility of scaling to a larger number of qubits using the trimon-type device. One direction is to increase the number of junctions in the loop to obtain more normal modes. An N-qubit device with all-to-all longitudinal coupling can be implemented with $N + 1$ junctions in the loop. However, as mentioned earlier, the frequency crowding and increased operational complexity might limit this approach to three to four qubits. Nevertheless, this kind of architecture might be suitable for

building quantum annealers which do not require dynamic control of interqubit coupling [16]. For conventional quantum computing, once can use the trimon as a three-qubit building block and can use existing techniques for coupling fixed-frequency transmon-type qubits [5,8] to build small-scale quantum processors. Another possibility is to use the trimon as a single qubit with switchable coupling to a cavity bus by exploiting the transfer-gate capability. This technique can help alleviate some of the problems related to residual coupling in such architectures.

Our experiments demonstrate a multimode superconducting quantum circuit which implements three quantum bits with strong, pairwise longitudinal coupling. The Purcell-protected qubits could potentially replace the standard transmon for many applications where a fast measurement is required without sacrificing qubit lifetime. We demonstrate the SWAP gate, which has several important applications, including quantum network architectures involving flying qubits [32] and, as an essential element of the Fredkin gate [33], a universal gate suitable for reversible computing. Extending to three qubits and using a single π pulse at $\omega_C^\mu - 2J_{CA} - 2J_{BC}$, we can implement the Toffoli gate [34,35], which is useful for quantum error correction. The demonstration of dipolar coupling to a nearby transmon qubit suggests that the trimon could be scaled up using existing multiqubit techniques [5,8] with the advantage of obtaining three qubits per block. Finally, the trimon concept can also be extended to circuits with a larger number of qubits with all-to-all coupling for applications in quantum annealing [16].

ACKNOWLEDGMENTS

APPENDIX A: HAMILTONIAN DERIVATION

The trimon device consists of four Josephson junctions (each with Josephson energy E_J) in a superconducting loop with four capacitor pads connected to each node. Besides capacitances C_C between adjacent node pairs (which

includes the intrinsic junction capacitance), these pads give rise to capacitances C_A and C_B between diagonal nodes, as shown in Fig. 5(a). This circuit provides three orthogonal oscillating modes [21]: two dipolar modes and a quadrupolar mode. The dipolar mode whose electric field is aligned with that of the 3D measurement cavity (the TE_{101} mode) is called the A mode. The second dipolar mode B, which is perpendicular to A, and the quadrupolar mode C ideally remain uncoupled from the cavity.

In order to derive the Hamiltonian for the system, we follow the approach used in [21] and define the node fluxes $\Phi_{\mu=1,2,3,4}$, which are related to the potentials ($V_{\mu=1,2,3,4}$) at circuit nodes 1,2,3,4 as

$$V_{\mu=1,2,3,4} = \frac{d\Phi_{\mu=1,2,3,4}}{dt} \equiv \dot{\Phi}_{\mu=1,2,3,4}. \tag{A1}$$

Note that we have used a cyclic convention for node numbering which is different from that used in Ref. [21]. In terms of these node fluxes, the capacitive energy in our device is

$$H_C = \sum_{\mu,\nu=1}^{4} \frac{1}{2} C_{\mu\nu} \dot{\Phi}_\mu \dot{\Phi}_\nu, \tag{A2}$$

where the capacitance matrix C is given by

$$C = \begin{pmatrix} 2C_C' + C_A & -C_C' & -C_A & -C_C' \\ -C_C' & 2C_C' + C_B & -C_C' & -C_B \\ -C_A & -C_C' & 2C_C' + C_A & -C_C' \\ -C_C' & -C_B & -C_C' & 2C_C' + C_B \end{pmatrix}. \tag{A3}$$

We ignore the capacitances of each pad to the ground and $C_C' = C_C + C_J$, where C_J is the intrinsic junction capacitance. The inductive energy of our circuit is

$$H_J = - \sum_{\mu=1,2,3,4} E_J \cos \delta_\mu, \tag{A4}$$

where E_J is the Josephson energy of each junction (assumed identical) and $\delta_{\mu=1,2,3,4}$ represent the gauge-invariant phase differences across the junctions satisfying the condition $(\delta_1 + \delta_2 + \delta_3 + \delta_4) \mod 2\pi = \Phi/\varphi_0$. Here, Φ is the total flux threading the loop and $\varphi_0 = \Phi_0/2\pi$ is the reduced flux quantum. We now write the junction phases in terms of the node fluxes as

$$\delta_1 = \frac{1}{\varphi_0}\left(\Phi_1 - \Phi_2 + \frac{\Phi}{4}\right), \tag{A5a}$$

$$\delta_2 = \frac{1}{\varphi_0}\left(\Phi_2 - \Phi_3 + \frac{\Phi}{4}\right), \tag{A5b}$$
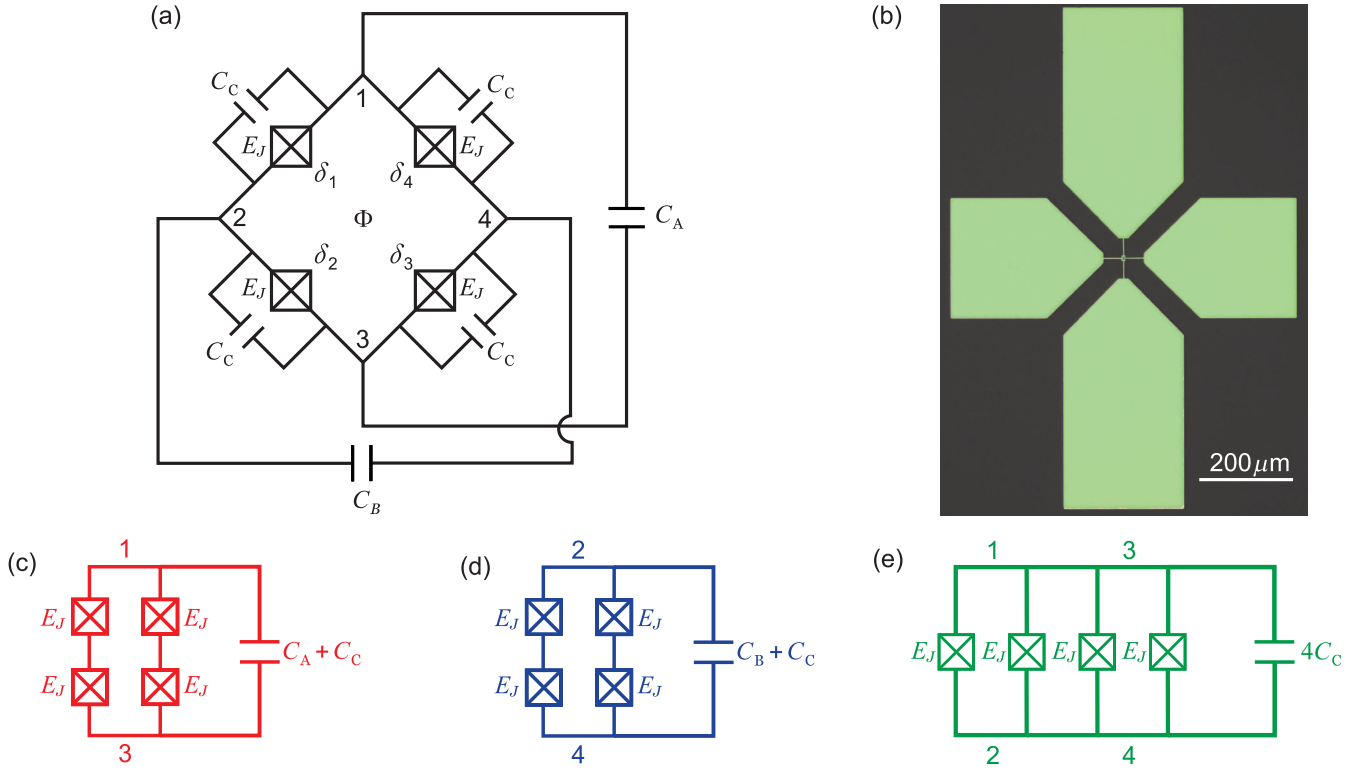
FIG. 5.   (a) Schematic circuit diagram of trimon device consisting of four Josephson junctions and six capacitors between four nodes. $\delta_{\mu=1,2,3,4}$ are the phase differences across the junctions with identical Josephson energies E_J. (b) False-colored optical image of the trimon device. (c)–(e) Effective circuit diagram for the A, B, and C modes.

$$\delta_3 = \frac{1}{\varphi_0}\left(\Phi_3 - \Phi_4 + \frac{\Phi}{4}\right), \tag{A5c}$$

$$\delta_4 = \frac{1}{\varphi_0}\left(\Phi_4 - \Phi_1 + \frac{\Phi}{4}\right). \tag{A5d}$$

In order to transform to the mode variable ($\Phi_{i=A,B,C}$), we use the following transformations:

$$\Phi_A = \Phi_1 - \Phi_3, \tag{A6a}$$

$$\Phi_B = \Phi_4 - \Phi_2, \tag{A6b}$$

$$\Phi_C = \frac{1}{2}(\Phi_1 - \Phi_2 + \Phi_3 - \Phi_4). \tag{A6c}$$

Note that the C-mode amplitude is defined differently [21] here so that the Hamiltonian of qubit C is identical to that of a standard transmon. Then the Josephson energy H_J of the circuit [21] simplifies to

$$H_J = -4E_J\left[\cos\left(\frac{\Phi_A}{2\varphi_0}\right)\cos\left(\frac{\Phi_B}{2\varphi_0}\right)\cos\left(\frac{\Phi_C}{\varphi_0}\right)\cos\left(\frac{\Phi}{4\varphi_0}\right)\right.$$
$$\left. + \sin\left(\frac{\Phi_A}{2\varphi_0}\right)\sin\left(\frac{\Phi_B}{2\varphi_0}\right)\sin\left(\frac{\Phi_C}{\varphi_0}\right)\sin\left(\frac{\Phi}{4\varphi_0}\right)\right], \tag{A7}$$

while the capacitive energy can be expressed as

$$\sum_{i=A,B,C}\frac{1}{2}\frac{e^2}{2E_{C_i}}\dot{\Phi}_i^2, \tag{A8}$$

where e is the electronic charge and the charging energies $E_{C_{i=A,B,C}}$ are given by

$$E_{C_A} = \frac{e^2}{2(C'_C + C_A)}, \qquad E_{C_B} = \frac{e^2}{2(C'_C + C_B)},$$

$$E_{C_C} = \frac{e^2}{8C'_C}. \tag{A9}$$

We now express the Hamiltonian of the full system using mode charge variables $Q_{i=A,B,C}$ (which are canonically conjugate to mode flux variable $\Phi_{i=A,B,C}$) for each mode and corresponding charging energies $E_{C_{i=A,B,C}}$,

$$H_{\text{circuit}} = H_J + \sum_{i=A,B,C} E_{C_i}\frac{Q_i^2}{e^2}. \tag{A10}$$

The magnitudes of $C_{i=A,B}$ are chosen to be unequal to lift the degeneracy between qubits A and B. Operating at zero applied flux ($\Phi = 0$), we expand Eq. (A10) up to fourth order in the mode amplitudes to get

$$H_{\text{circuit}} = -4E_J + \left(E_{C_A} q_A^2 + \frac{E_J}{2} \phi_A^2 - \frac{E_J}{96} \phi_A^4 \right)$$
$$+ \left(E_{C_B} q_B^2 + \frac{E_J}{2} \phi_B^2 - \frac{E_J}{96} \phi_B^4 \right)$$
$$+ \left(E_{C_C} q_C^2 + \frac{4E_J}{2} \phi_C^2 - \frac{E_J}{6} \phi_C^4 \right)$$
$$- \frac{E_J}{16} (\phi_A^2 \phi_B^2 + 4\phi_B^2 \phi_C^2 + 4\phi_C^2 \phi_A^2), \quad \text{(A11)}$$

where $q_i = Q_i/e$ and $\phi_i = \Phi_i/\varphi_0$. Here, each qubit is expressed as a weakly anharmonic oscillator. While qubit C looks like a regular transmon, the qubits A and B show reduced nonlinearity. This is because in qubit C (quadrupole), all of the junctions are effectively in parallel, while qubits A and B have two junctions in series [Figs. 5(c)–5(e)]. As we will see later, this design dilutes the anharmonicity of A and B by a factor of 4. We now quantize the circuit by introducing the bosonic raising and lowering operators, which are related to the flux and charge operators as

$$\Phi_i = \sqrt{\frac{\hbar Z_i}{2}} (a_i^\dagger + a_i), \quad \text{(A12a)}$$

$$Q_i = i \sqrt{\frac{\hbar}{2Z_i}} (a_i^\dagger - a_i). \quad \text{(A12b)}$$

We define the uncoupled mode frequencies and mode impedances as

$$\omega_A = \frac{\sqrt{8E_J E_{C_A}}}{\hbar}, \qquad Z_A = \frac{\hbar}{e^2} \sqrt{\frac{E_{C_A}}{2E_J}}, \quad \text{(A13a)}$$

$$\omega_B = \frac{\sqrt{8E_J E_{C_B}}}{\hbar}, \qquad Z_B = \frac{\hbar}{e^2} \sqrt{\frac{E_{C_B}}{2E_J}}, \quad \text{(A13b)}$$

$$\omega_C = \frac{\sqrt{32E_J E_{C_C}}}{\hbar}, \qquad Z_C = \frac{\hbar}{e^2} \sqrt{\frac{E_{C_C}}{8E_J}}. \quad \text{(A13c)}$$

Then the effective Hamiltonian under rotating-wave approximation becomes

$$\frac{1}{\hbar} H_{\text{eff}} = \sum_{i=A,B,C} [(\omega_i - \beta_i) a_i^\dagger a_i - J_i a_i^\dagger a_i a_i^\dagger a_i]$$
$$- \sum_{i \neq j} 2J_{ij} a_i^\dagger a_i a_j^\dagger a_j, \quad \text{(A14)}$$

with

$$\beta_i = J_i + J_{ij} + J_{ki}, \qquad i \neq j \neq k, \quad \text{(A15a)}$$

$$J_A = \frac{E_{C_A}}{8\hbar}, \qquad J_B = \frac{E_{C_B}}{8\hbar}, \qquad J_C = \frac{E_{C_C}}{2\hbar}, \quad \text{(A15b)}$$

$$J_{AB} = \frac{\sqrt{E_{C_A} E_{C_B}}}{4\hbar},$$
$$J_{BC} = \frac{\sqrt{E_{C_B} E_{C_C}}}{2\hbar},$$
$$J_{CA} = \frac{\sqrt{E_{C_C} E_{C_A}}}{2\hbar}, \quad \text{(A15c)}$$

where J_i and J_{ij} are the coupling coefficients for the self-Kerr (Φ_i^4) and pairwise cross-Kerr ($\Phi_i^2 \Phi_j^2$) terms, respectively. Using second-order perturbation theory, one finds the energy eigenstates of the system to be

$$\frac{1}{\hbar} E_{n_A, n_B, n_C} = \sum_{i=A,B,C} [(\omega_i - \beta_i) n_i - J_i n_i^2] - \sum_{i \neq j} 2J_{ij} n_i n_j. \quad \text{(A16)}$$

Using Eq. (A16), we compute the anharmonicities [9] of the individual modes:

$$\alpha_A = -\frac{E_{C_A}}{4\hbar}, \qquad \alpha_B = -\frac{E_{C_B}}{4\hbar}, \qquad \alpha_C = -\frac{E_{C_C}}{\hbar}. \quad \text{(A17)}$$

As mentioned earlier, only the anharmonicity of the qubit C is identical to that of a transmon, while those of qubits A and B are diluted by a factor of 4. However, in this device, $E_{C_C} \sim E_{C_{A,B}}/4$, and hence the anharmonicities of all three qubits are similar.

Restricting ourselves to the four lowest-energy eigenstates of Eq. (A22), we write the Hamiltonian in terms of Pauli spin matrices as

$$\frac{1}{\hbar} H_{\text{spin}} = -\frac{1}{2} \left[\sum_{i=A,B,C} (\omega_i - 2\beta_i) \sigma_z^i + \sum_{i \neq j} J_{ij} \sigma_z^i \sigma_z^j \right], \quad \text{(A18)}$$

where

$$\beta_i = J_i + J_{ij} + J_{kj}, \qquad i \neq j \neq k. \quad \text{(A19)}$$

As a result, each qubit now has four possible values of transition frequency, depending upon the state of its partner qubits:

$$\omega_A^{B=s,C=t} = \omega_A - 2\beta_A + (-1)^s J_{AB} + (-1)^t J_{CA}, \qquad s,t \in \{0,1\}, \tag{A20a}$$

$$\omega_B^{C=s,A=t} = \omega_B - 2\beta_B + (-1)^s J_{BC} + (-1)^t J_{AB}, \qquad s,t \in \{0,1\}, \tag{A20b}$$

$$\omega_C^{A=s,B=t} = \omega_C - 2\beta_C + (-1)^s J_{CA} + (-1)^t J_{BC}, \qquad s,t \in \{0,1\}. \tag{A20c}$$

Since qubit C is kept in its ground state in our experiment, qubits A and B have only two transition frequencies each. We call them the upper ($\omega_{A,B}^u$) and lower ($\omega_{A,B}^l$) band frequencies [see Fig. 1(d) in the main text] and are given by

$$\omega_A^u = \omega_A^{B=0,C=0} = \omega_A - 2J_A - J_{AB} - J_{CA}, \tag{A21a}$$

$$\omega_A^l = \omega_A^{B=1,C=0} = \omega_A - 2J_A - 3J_{AB} - J_{CA}, \tag{A21b}$$

$$\omega_B^u = \omega_B^{C=0,A=0} = \omega_B - 2J_B - J_{AB} - J_{BC}, \tag{A21c}$$

$$\omega_B^l = \omega_B^{C=0,A=1} = \omega_B - 2J_B - 3J_{AB} - J_{BC}. \tag{A21d}$$

Including the interaction with the host cavity, we write the Hamiltonian of the full system as

$$\frac{1}{\hbar} H_{system} = -\frac{1}{2} \left[\sum_{i=A,B,C} (\omega_i - 2\beta_i)\sigma_z^i + \sum_{i \neq j} J_{ij}\sigma_z^i \sigma_z^j \right]$$
$$+ \left(\omega_{cav} - \sum_{i=A,B,C} \chi_i \sigma_z^i \right) a^\dagger a, \tag{A22}$$

where the dispersive shifts [9] for the three qubits are given by

$$\chi_A = g^2 \left(\frac{1}{\Delta_0} - \frac{1}{\Delta_1} \right), \tag{A23a}$$

$$\chi_B = \frac{g^2}{2} \left(\frac{1}{\Delta_0} - \frac{1}{\Delta_0 - 2J_{AB}} \right), \tag{A23b}$$

$$\chi_C = \frac{g^2}{2} \left(\frac{1}{\Delta_0} - \frac{1}{\Delta_0 - 2J_{CA}} \right). \tag{A23c}$$

Here, g is the coupling between qubit A and cavity $\omega_{cav} = \omega_{bare} - g^2/\Delta_0 + \sum_i \chi_i$, with ω_{bare} being the bare resonant frequency of the cavity, $\Delta_0 = \omega_A^u - \omega_{bare}$, and $\Delta_1 = \Delta_0 + \alpha_A$. Although each of the qubits has its own dispersive shift on the cavity, their origins are quite different. While qubit A has the usual dispersive shift [9] due to the coupling to the cavity, one expects that the dispersive shifts of qubits B and C should be zero since they

are completely decoupled from it. However, when qubit B (C) is excited, the transition frequency of qubit A is shifted via the $\sigma_z^A \sigma_z^B$ ($\sigma_z^C \sigma_z^A$) term. This change in qubit A's frequency leads to a dispersive shift in the cavity frequency since the detuning between qubit A and the cavity changes. Interestingly, for our typical device parameters, this indirect dispersive shift for B (C) qubit is similar in magnitude to the regular dispersive shift for qubit A.

It is possible to tune the transition frequencies of the three qubits by threading a nonzero flux through the JRM loop. However, the second term of Eq. (A7) will be nonzero and introduce additional interqubit coupling terms. The dominant term will be the pure mixing term ($\propto \Phi_A \Phi_B \Phi_C$), which has previously been exploited for parametric amplification [21,22,36]. However, this term is ineffective since the qubit frequencies are off resonant. Note that this three-body coupling term is at the heart of parametric amplification using the JRM and is activated when one mode is pumped at the sum of the other two mode frequencies. This is, however, not the case here at all. We plan to explore this regime of operation in the future where one can do gate operations by parametric pumping techniques. In practice, we have been able to tune the qubit transition frequencies down by about 200 MHz before the JRM experiences a jump to a different flux branch, as expected, and makes the device unstable. If one needs larger frequency tuning in such a device, the single Josephson junctions can be replaced with superconducting quantum-interference devices (SQUIDs) with a smaller loop area than the JRM. This way, one can tune the effective E_J while operating at integer flux quantum in the JRM loop.

Experimentally measured anharmonicities (see Table I in the main text) are used to obtain the values of $E_{C_{i=A,B,C}}$ using Eq. (A17), and hence the values of couplings J_{ij} using Eq. (A15c). Dispersive shifts of the qubits are calculated using Eq. (A23). The comparison between theoretical and experimentally obtained values of these parameters for sample D1 are given in Table II. The agreement between theory and experiment for J_{ij} is quite reasonable given that we have not accounted for the variability in the Josephson energies (E_J) of the four junctions in the JRM. These variations will introduce additional terms in the Hamiltonian

TABLE II. Comparison of various device parameters between theory and experiment.

(In MHz)	J_{AB}/π	J_{BC}/π	J_{CA}/π	$\chi_A/2\pi$	$\chi_B/2\pi$	$\chi_C/2\pi$
Theory	227.0	253.6	248.0	−0.332	−0.279	−0.317
Experiment	201.2	253.0	232.0	−0.332	−0.376	−0.386

TABLE III.   Parameters and coherence properties of the trimon in the presence of a neighboring transmon. The transition frequency (ω^u) of each qubit with the other two qubits in their ground state is listed along with the anharmonicity (α), relaxation time (T_1), Hahn-echo time (T_2^E), and interqubit coupling strength (J_{ij}).

Qubit	$\omega^u/2\pi$ (GHz)	$\alpha/2\pi$ (MHz)	T_1 (μs)	T_2^E (μs)	J_{ij}/π (MHz)
A	4.5590	−118	32.0	44	$J_{AB}/\pi = 203.0$
B	5.0578	−120	50.5	78	$J_{BC}/\pi = 272.0$
C	5.8073	−144	25.0	47	$J_{CA}/\pi = 236.0$

and result in small changes in theoretical predictions. The disagreement for $\chi_{B,C}$ is much larger and requires further investigation. We notice similar agreement between theory and experiment across several samples. The effect of variability in E_J and the inclusion of higher-order spin interaction terms will be the subject of a future manuscript.

APPENDIX B: MEASUREMENT SETUP AND PULSE-GENERATION TECHNIQUE

The measurement setup is shown in Fig. 6. Readout is performed in transmission mode, where the output signal is first amplified by a near-quantum-limited LJPA [27]
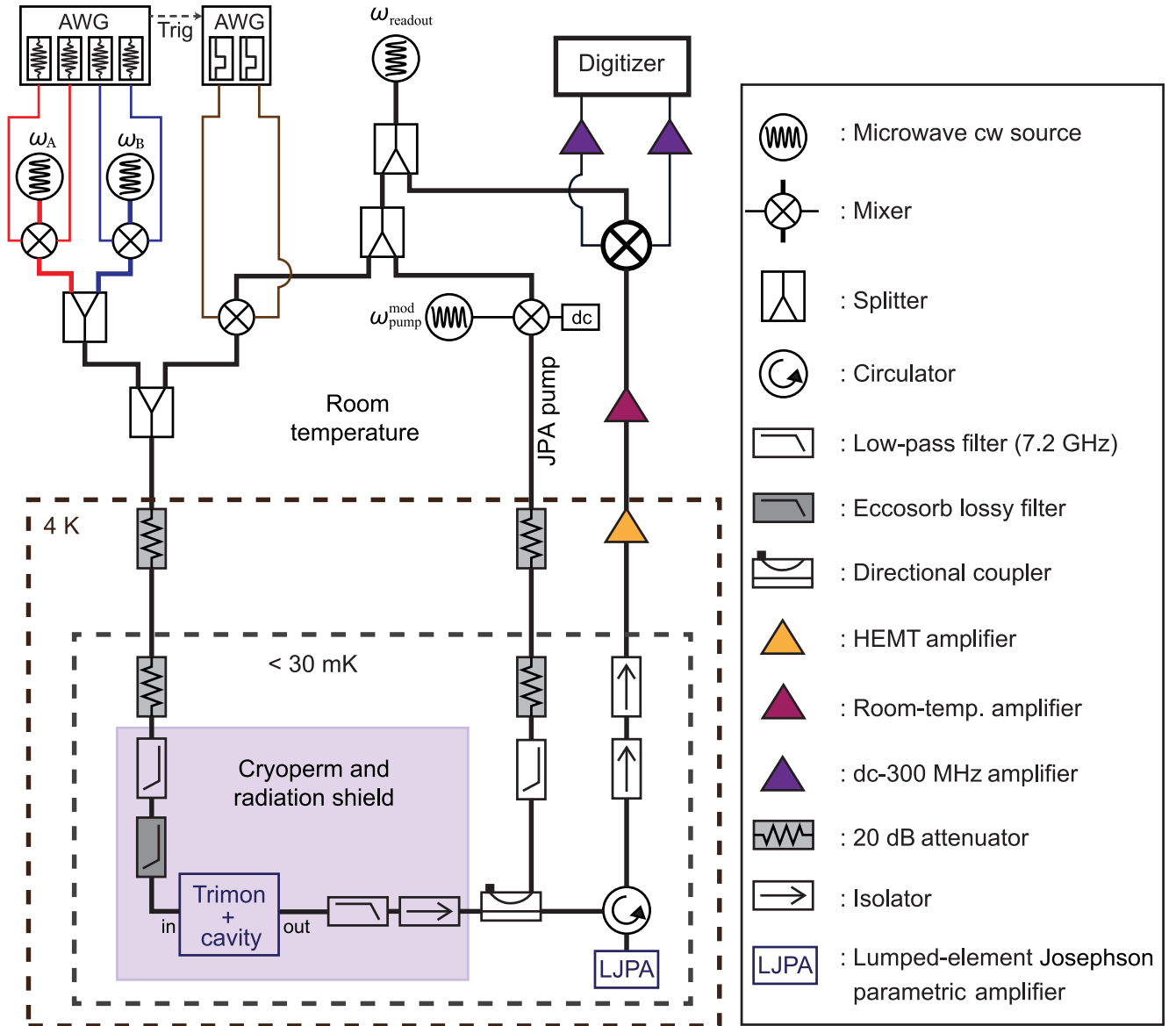

FIG. 6.   Room-temperature signal generation and detection setup along with cryogenic wiring and filtering.

at base temperature, followed by cryogenic (4-K) and room-temperature low-noise amplifiers. Input lines are heavily attenuated and filtered using reflective low-pass and lossy Eccosorb® filters [37]. We use three microwave sources, two for the qubits (A and B, respectively) and one for readout. The upper- and lower-band frequencies for each qubit is generated using a sideband modulation technique where the local oscillator for the mixer is set to the mean frequency: $(\omega_{i=A,B}^u + \omega_{i=A,B}^l)/2$. The in-phase (I) and quadrature-phase (Q) modulating signals (at frequency J_{AB}) are generated using a 1×10^9 samples/s arbitrary waveform generator (AWG) with a 300-MHz analog bandwidth. The amplitude and phase of these signals are optimized to create either a single-tone ($\omega_{A,B}^u$ or $\omega_{A,B}^l$) signal for conditional rotations or a multitone signal ($\omega_{A,B}^u$ and $\omega_{A,B}^l$) for qubit selective rotations. The signal strengths on each band for a given qubit are adjusted to provide identical pulse lengths for a given rotation angle. We use Gaussian-edge, flat-top pulses to have a good balance between pulse bandwidth and pulse lengths.

One particular advantage of this technique is the simple control of rotation axis by adjusting the phase of the modulating signal in software. Additionally, any rotation of the qubit about Z axis does not require a separate gate and can be included by modifying the rotation axis of subsequent pulses. One important detail in this technique is to ensure that the phase difference between the upper- and lower-band tones for qubit A must be identical to that of qubit B. This difference can arise due to the unequal cable lengths at the rf output of the IQ mixers before they are combined and sent to the device. However, this phase difference can be easily compensated for by adjusting the phase of the quadrature modulating signals as well. This technique can easily be extended for a three-qubit system, where four tones per qubit would be generated using appropriate modulating signals.

APPENDIX C: COUPLING OF THREE QUBITS TO THE CAVITY

In the trimon with identical Josephson junctions, only qubit A couples to the cavity with coupling strength g_A. In order to estimate the spurious coupling of qubits B and C to the cavity (g_B and g_C) due to junction asymmetries, we used the data shown in Figs. 4(b)–4(d) in the main text for device D2. The relative coupling strengths of the different qubits to the transmon can be used as a rough estimate for their relative coupling strengths to the cavity. We obtain $g_B \sim g_A/10$ and $g_C \sim g_A/20$, which are small enough to ensure that the relaxation time for qubits B and C is not limited by the Purcell effect [38], provided their transition frequencies are not too close to the cavity's resonance. Furthermore,

the presence of an off-resonant qubit [the transmon in Fig. 4(a) in the main text] does not degrade the coherence times of the trimon. Coherence numbers for the three qubits residing in the trimon of device D2 are given in Table III.

The relatively small coupling of qubits B and C to the cavity makes it very difficult to couple power into those qubits and is the primary reason behind our gate pulse lengths being relatively long. It should be possible to carefully tailor the power coupling by introducing controlled asymmetry in the junctions or by redesigning port configuration on the cavity. The large power required to drive qubit C also results in a strong ac Stark shift [39] and prevents us from obtaining a clear Hahn-echo signal (see Table I in the main text).

APPENDIX D: MATRIX REPRESENTATION OF CONDITIONAL ROTATIONS

The two-qubit states $|AB\rangle$ residing in a four-dimensional Hilbert space are represented by the basis

$$|00\rangle = \begin{pmatrix} 1 \\ 0 \\ 0 \\ 0 \end{pmatrix}, \qquad |01\rangle = \begin{pmatrix} 0 \\ 1 \\ 0 \\ 0 \end{pmatrix},$$

$$|10\rangle = \begin{pmatrix} 0 \\ 0 \\ 1 \\ 0 \end{pmatrix}, \qquad |11\rangle = \begin{pmatrix} 0 \\ 0 \\ 0 \\ 1 \end{pmatrix}. \tag{D1}$$

The controlled rotations of qubit B in a plane making an angle ϕ with the x-z plane conditioned when $A = |1\rangle$ (the lower band) and $A = |0\rangle$ (the upper band) are given by

$$\mathcal{R}_{Bl}(\phi, \theta) = \begin{pmatrix} 1 & 0 & 0 & 0 \\ 0 & 1 & 0 & 0 \\ 0 & 0 & \cos(\theta/2) & -e^{-i\phi}\sin(\theta/2) \\ 0 & 0 & e^{i\phi}\sin(\theta/2) & \cos(\theta/2) \end{pmatrix},$$

$$\mathcal{R}_{Bu}(\phi, \theta) = \begin{pmatrix} \cos(\theta/2) & -e^{-i\phi}\sin(\theta/2) & 0 & 0 \\ e^{i\phi}\sin(\theta/2) & \cos(\theta/2) & 0 & 0 \\ 0 & 0 & 1 & 0 \\ 0 & 0 & 0 & 1 \end{pmatrix}. \tag{D2}$$

Similarly controlled rotations for qubit A conditional on the state of qubit B are given by

$$\mathcal{R}_{Al}(\phi,\theta) = \begin{pmatrix} 1 & 0 & 0 & 0 \\ 0 & \cos(\theta/2) & 0 & -e^{-i\phi}\sin(\theta/2) \\ 0 & 0 & 1 & 0 \\ 0 & e^{i\phi}\sin(\theta/2) & 0 & \cos(\theta/2) \end{pmatrix},$$

$$\mathcal{R}_{Au}(\phi,\theta) = \begin{pmatrix} \cos(\theta/2) & 0 & -e^{-i\phi}\sin(\theta/2) & 0 \\ 0 & 1 & 0 & 0 \\ e^{i\phi}\sin(\theta/2) & 0 & \cos(\theta/2) & 0 \\ 0 & 0 & 0 & 1 \end{pmatrix}.$$

$$(D3)$$

These rotations can be used to implement generic two-qubit controlled unitary gates. The conventional CNOT gate (up to a $-90°$ phase) becomes a special case of these controlled rotations, namely, $\mathcal{R}_{Bl}(-\pi/2,\pi) = \mathcal{R}_{Bl,x}(\pi) = -i\text{CNOT}_{AB}$ and $\mathcal{R}_{Al}(-\pi/2,\pi) = \mathcal{R}_{Al,x}(\pi) = -i\text{CNOT}_{BA}$, where $\phi = -\pi/2$ denotes rotation about the x axis.

APPENDIX E: SINGLE-QUBIT RANDOMIZED BENCHMARKING

In order to characterize single-qubit gate fidelities, we perform randomized benchmarking for qubits A and B using the protocol described by Chow *et al.* [30]. The average gate fidelities of qubits A and B as a function of the number of computational gates are shown in Fig. 7. Each computational gate consists of a randomized Pauli gate and a randomized Clifford generator, both comprising two pulses at upper and lower bands, generated using the sideband modulation technique
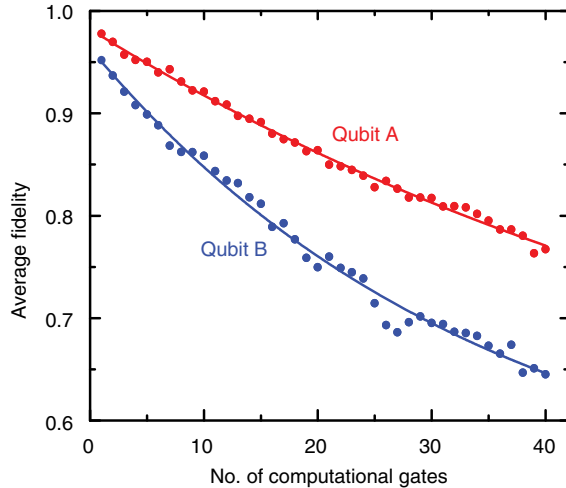

FIG. 7.   Average gate fidelity vs number of randomized computational gates for qubits A (red) and B (blue). Solid dots are the experimentally obtained data after 180 000 averages. Fits to the data (solid lines) show mean fidelities of 0.9928 ± 0.0001 and 0.9858 ± 0.0002 for qubits A and B, respectively.

described in Appendix B. Each sequence of random gates is preceded by a strong measurement in order to herald the $|000\rangle$ state.

APPENDIX F: TWO-QUBIT STATE TOMOGRAPHY

For a two-qubit system, the density matrix (ρ) can be constructed by a set of 16 linearly independent operators $\{O_i\}$:

$$\rho = \sum_{i=0}^{15} c_i O_i. \qquad (F1)$$

The goal of tomography is to determine the set of coefficients $\{c_i\}$ from the expectation values of the observables $\{O_i\}$. One such set is the Kronecker product of the Pauli matrices σ_i,

$$\rho = \frac{1}{4}\sum_{i,j=x,y,z,0} S_{ij}\sigma_i \otimes \sigma_j. \qquad (F2)$$

The coefficients S_{ij} are called the Stokes parameters. From trace normalization S_{00} should always be unity. The problem then reduces to estimating the remaining 15 coefficients from the results of six single-qubit measurements of the type $\sigma_i \otimes \mathcal{I}$ or $\mathcal{I} \otimes \sigma_i$ and nine two-qubit measurements of the type $\sigma_i \otimes \sigma_j$, where $\{i,j = x,y,z\}$.

The generic form of our two-qubit joint measurement operator can be written as [40]

$$O = \beta_0 + \beta_1\sigma_z^A + \beta_2\sigma_z^B + \beta_{12}\sigma_z^A \otimes \sigma_z^B. \qquad (F3)$$

Since our measurement operator involves both one- and two-qubit observables, the complete set of independent observables can be obtained by applying single-qubit rotations prior to the measurements [41].

We use the standard MLE technique [42,43] to reconstruct the density matrices. MLE searches in the parameter space of all physical density matrices and finds the density matrix ρ which is most likely to have produced the observed experimental data $\mathcal{D}$ by constructing the likelihood functional. The likelihood functional is a probability distribution for obtaining the measured data given a state ρ; hence, it is a function of the independent parameters characterizing the density matrix. For all physical states, the density matrix can be written as the Cholesky decomposed form

$$\rho = \frac{\mathcal{T}^\dagger\mathcal{T}}{\text{Tr}[\mathcal{T}^\dagger\mathcal{T}]}, \qquad (F4)$$

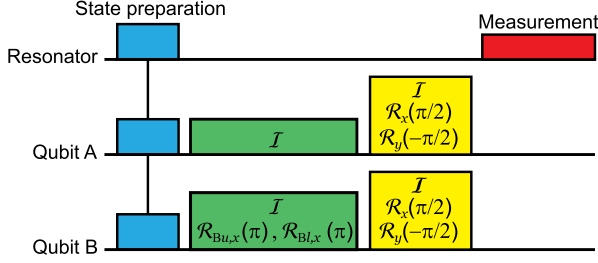where $\mathcal{T}$ is an upper-triangular matrix given by

FIG. 8.   Pulse sequence for tomography. State preparation (the blue boxes) involves the strong measurement for selecting the initial $|000\rangle$ state (heralding), followed by pulses to initialize the two-qubit state. With the default measurement direction being the z axis, measurements along the x and y axes for each qubit are done by performing prerotations by $-\pi/2$ along the y axis and $\pi/2$ along the x axis, respectively. The yellow boxes represent nine possible prerotations and, ideally, should form a complete set for tomography. However, in our experiments, distributions for states $|01\rangle$ and $|10\rangle$ are largely overlapping (see Fig. 9), but distinguishable from those of $|00\rangle$ and $|11\rangle$. In order to differentiate $|01\rangle$ and $|10\rangle$, we repeat the same sequence with two controlled rotations prior to the prerotations transferring populations to $|00\rangle$ and $|11\rangle$, respectively.

$$\mathcal{T} = \begin{bmatrix} t_1 & t_5 - it_6 & t_{11} - it_{12} & t_{15} - it_{16} \\ 0 & t_2 & t_7 - it_8 & t_{13} - it_{14} \\ 0 & 0 & t_3 & t_9 - it_{10} \\ 0 & 0 & 0 & t_4 \end{bmatrix}. \quad (F5)$$

The likelihood functional is defined as

$$\mathcal{L}(\mathcal{D}_k|\rho\{t_i\}) = \prod_{k=1}^{16} \mathcal{P}(\mathcal{D}_k|\rho\{t_i\}) = \prod_{k=1}^{16} [\langle\psi_k|\rho(t_i)|\psi_k\rangle]^{f_k}. \quad (F6)$$

Here, $\mathcal{P}(\mathcal{D}_k|\rho\{t_i\})$ is the probability of having the measurement data $\mathcal{D}_k$ corresponding to the kth measurement given the density matrix $\rho\{t_i\}$. The term $\langle\psi_k|\rho\{t_i\}|\psi_k\rangle$ denotes the probability of having the kth state, and f_k is the occurrence frequency of that state in an experiment. We can further simplify the expression if we assume Gaussian counting statistics and define the log-likelihood functional as

$$\mathbb{L}(\mathcal{D}_k|\rho\{t_i\}) = \log L(\mathcal{D}_k|\rho\{t_i\})$$
$$= -\sum_{k=1}^{16} \frac{(\langle\psi_k|\rho\{t_i\}|\psi_k\rangle - f_k)^2}{2\langle\psi_k|\rho\{t_i\}|\psi_k\rangle}, \quad (F7)$$

where we have set any proportionality constant to unity. Our goal is then to maximize this function with respect to the parameters $\{t_i\}$.

In our setup, the measurement is implemented by sending a microwave pulse at the cavity frequency. The signal transmitted through the cavity acquires a phase shift which is dependent on the joint state of the two qubits. This signal is first amplified by a near-quantum-limited LJPA [27], followed by more amplification using a cryogenic (4 K) HEMT amplifier and a room-temperature low-noise amplifier. The amplified signal is then demodulated using the homodyne technique and digitized. The digitized signal is integrated for 700 ns to create one measurement result (V_p), and repeating this process several thousand times allows us to create a population histogram, as shown in Fig. 9(a).

The occurrence frequencies f_k are obtained from the population histograms with different prerotations, as shown in Fig. 8. In our experimental setup, the histograms corresponding to $|00\rangle$ and $|11\rangle$ are well separated from each other and also from $|01\rangle$ and $|10\rangle$, but the latter
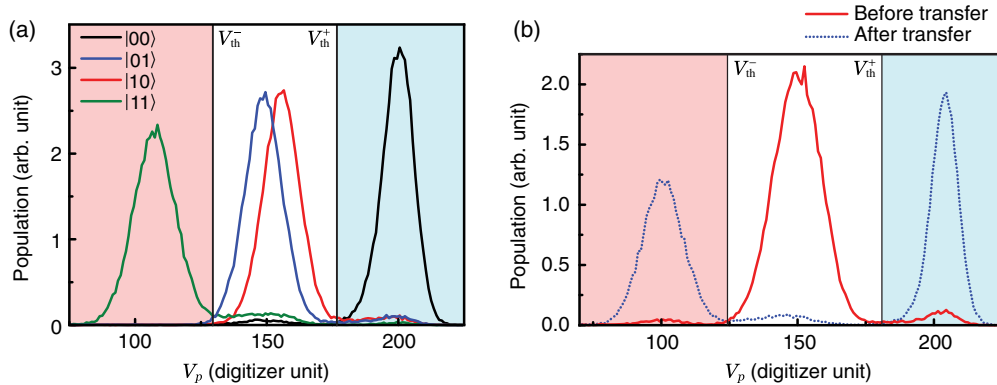

FIG. 9.   (a) Population histograms corresponding to individual states $|00\rangle$ (the black line), $|10\rangle$ (the red line), $|01\rangle$ (the blue line), and $|11\rangle$ (the green line), with thresholds V_{th}^+ and V_{th}^-. Any outcome above the threshold V_{th}^+ (the light-blue shaded region) is registered as the $|00\rangle$ state. (b) Histograms of measurement results (V_p) for the state $(|01\rangle + |10\rangle)/\sqrt{2}$. Outcomes $V_p < V_{\mathrm{th}}^-$ and $V_p > V_{\mathrm{th}}^+$ are considered to be in the states $|11\rangle$ and $|00\rangle$, respectively. The red histogram shows an overlapping distribution of states $|01\rangle$ and $|10\rangle$ before population transfer, and the dashed blue histogram depicts the outcome after application of the controlled-rotations, thereby making them distinguishable.

two are largely overlapping and hence indistinguishable [see Fig. 9(a)]. This is because of similar values for χ_A and χ_B (see Table II). The measurement result is identified as the state $|00\rangle$ or $|11\rangle$ depending on whether V_p is above or below some appropriately chosen thresholds V_{th}^+ and V_{th}^-, as shown in Fig. 9. All other values of V_p between these two thresholds are discarded. In order to obtain the population corresponding to $|01\rangle$ and $|10\rangle$, we perform an additional measurement set by applying two controlled rotations prior to the single-qubit rotations. These two pulses exchange the population $|01\rangle \leftrightarrow |00\rangle$ and $|10\rangle \leftrightarrow |11\rangle$, making them distinguishable. We keep the same thresholds V_{th}^+ and V_{th}^- to digitize the result. The schematic of the tomographic pulse sequence is shown in Fig. 8.

We determine the density matrix ρ of the two-qubit system by measuring the state along all 9 basis directions

(a) Re($\rho_{initial}$) (b) Im($\rho_{initial}$)
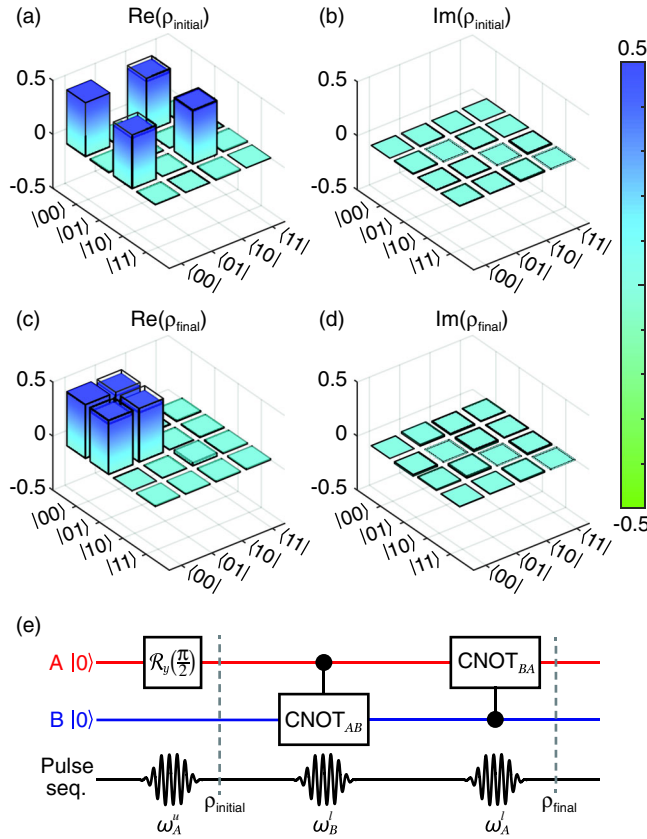(c) Re(ρ_{final}) (d) Im(ρ_{final})

(e)

FIG. 10. We initialize the two-qubit state in $[(|0\rangle + |1\rangle)/\sqrt{2}]_A \otimes |0\rangle_B$ with the fidelity 0.984 ± 0.005 and apply a transfer gate to obtain the final state $|0\rangle_A \otimes [(|0\rangle + |1\rangle)/\sqrt{2}]_B$ with the fidelity 0.973 ± 0.005. (a),(b) Real and imaginary components of the reconstructed density matrices before transfer and (c),(d) after transfer. Here, filled colored bars are the experimental data, while transparent bars with black boundaries denote ideal values corresponding to the intended state. (e) Quantum circuit for the transfer protocol and the corresponding pulse sequence. The $\pi/2$ pulse at ω_A^u is 152 ns long; pulse lengths for CNOT$_{AB}$ and CNOT$_{BA}$ are 497 and 241 ns, respectively.

performed by applying appropriate single-qubit prerotations. Any particular single qubit observable is measured by tracing over outcomes of the other qubit. Since the population histograms will always have some overlap with each other, the tail of the distribution beyond the threshold will lead to an incorrect detection of a measurement result and will, eventually, reduce fidelity of the reconstructed density matrix. The fidelity numbers quoted in the main text and in Fig. 10 are thus limited by these finite overlaps.

We would like to add that the density matrix is first computed by the "forced purity" method [44] (which is much faster than MLE, but not very accurate), and its outcome is used to initialize the search in parameter space to obtain the density matrix ρ_{MLE}. The fidelity to the target state (ρ_{th}) is calculated using the formula

$$\mathcal{F}(\rho_{th}, \rho_{MLE}) = \mathrm{Tr}\left[\sqrt{\sqrt{\rho_{th}}\rho_{MLE}\sqrt{\rho_{th}}}\right]. \quad \text{(F8)}$$

APPENDIX G: TRANSFER GATE

Transfer gate is a special case of SWAP gate where the target qubit is initialized to its ground state and can be accomplished using only two CNOT gates on the two participant qubits. We demonstrate transfer of the state $(|0\rangle + |1\rangle)/\sqrt{2}$ from qubit A to B. The reconstructed density matrices before and after the transfer gate along with the pulse protocol are shown in Fig. 10. The initial state $[(|0\rangle + |1\rangle)/\sqrt{2}]_A \otimes |0\rangle_B$ is prepared with the fidelity 0.984 ± 0.005, while the final state $|0\rangle_A \otimes [(|0\rangle + |1\rangle)/\sqrt{2}]_B$ after the transfer showed a fidelity of 0.973 ± 0.005.

[1] M. H. Devoret and R. J. Schoelkopf, Superconducting circuits for quantum information: An outlook, Science **339**, 1169 (2013).

[2] J. Kelly *et al.*, State preservation by repetitive error detection in a superconducting quantum circuit, Nature (London) **519**, 66 (2015).

[3] A. D. Córcoles, Easwar Magesan, Srikanth J. Srinivasan, Andrew W. Cross, M. Steffen, Jay M. Gambetta, and Jerry M. Chow, Demonstration of a quantum error detection code using a square lattice of four superconducting qubits, Nat. Commun. **6**, 6979 (2015).

[4] D. Ristè, S. Poletto, M.-Z. Huang, A. Bruno, V. Vesterinen, O.-P. Saira, and L. DiCarlo, Detecting bit-flip errors in a logical qubit using stabilizer measurements, Nat. Commun. **6**, 6983 (2015).

[5] J. Z. Blumoff, K. Chou, C. Shen, M. Reagor, C. Axline, R. T. Brierley, M. P. Silveri, C. Wang, B. Vlastakis, S. E. Nigg, L. Frunzio, M. H. Devoret, L. Jiang, S. M. Girvin, and R. J. Schoelkopf, Implementing and Characterizing Precise Multiqubit Measurements, Phys. Rev. X **6**, 031041 (2016).

[6] R. Barends *et al.*, Digital quantum simulation of fermionic models with a superconducting circuit, Nat. Commun. **6**, 7654 (2015).

[7] Y. Salathé, M. Mondal, M. Oppliger, J. Heinsoo, P. Kurpiers, A. Potočnik, A. Mezzacapo, U. Las Heras, L. Lamata, E. Solano, S. Filipp, and A. Wallraff, Digital Quantum Simulation of Spin Models with Circuit Quantum Electrodynamics, Phys. Rev. X **5**, 021027 (2015).

[8] Hanhee Paik, A. Mezzacapo, Martin Sandberg, D. T. McClure, B. Abdo, A. D. Córcoles, O. Dial, D. F. Bogorin, B. L. T. Plourde, M. Steffen, A. W. Cross, J. M. Gambetta, and Jerry M. Chow, Experimental Demonstration of a Resonator-Induced Phase Gate in a Multiqubit Circuit-QED System, Phys. Rev. Lett. **117**, 250502 (2016).

[9] Jens Koch, Terri M. Yu, Jay Gambetta, A. A. Houck, D. I. Schuster, J. Majer, Alexandre Blais, M. H. Devoret, S. M. Girvin, and R. J. Schoelkopf, Charge-insensitive qubit design derived from the Cooper pair box, Phys. Rev. A **76**, 042319 (2007).

[10] Yuriy Makhlin, Gerd Scöhn, and Alexander Shnirman, Josephson-junction qubits with controlled couplings, Nature (London) **398**, 305 (1999).

[11] J. Q. You, J. S. Tsai, and Franco Nori, Scalable Quantum Computing with Josephson Charge Qubits, Phys. Rev. Lett. **89**, 197902 (2002).

[12] Andrew J. Kerman, Quantum information processing using quasiclassical electromagnetic interactions between qubits and electrical resonators, New J. Phys. **15**, 123011 (2013).

[13] Baptiste Royer, Arne L. Grimsmo, Nicolas Didier, and Alexandre Blais, Fast and high-fidelity entangling gate through parametrically modulated longitudinal coupling, arXiv:1603.04424.

[14] P.-M. Billangeon, J. S. Tsai, and Y. Nakamura, Scalable architecture for quantum information processing with superconducting flux qubits based on purely longitudinal interactions, Phys. Rev. B **92**, 020509 (2015).

[15] Susanne Richer and David DiVincenzo, Circuit design implementing longitudinal coupling: A scalable scheme for superconducting qubits, Phys. Rev. B **93**, 134501 (2016).

[16] Martin Leib, Peter Zoller, and Wolfgang Lechner, A transmon quantum annealer: Decomposing many-body Ising constraints into pair interactions, Quantum Sci. Technol. **1**, 015008 (2016).

[17] J. M. Gambetta, A. A. Houck, and Alexandre Blais, Superconducting Qubit with Purcell Protection and Tunable Coupling, Phys. Rev. Lett. **106**, 030502 (2011).

[18] I. Diniz, E. Dumur, O. Buisson, and A. Auffèves, Ultrafast quantum nondemolition measurements based on a diamond-shaped artificial atom, Phys. Rev. A **87**, 033837 (2013).

[19] Anthony J. Hoffman, Srikanth J. Srinivasan, Jay M. Gambetta, and Andrew A. Houck, Coherent control of a superconducting qubit with dynamically tunable qubit-cavity coupling, Phys. Rev. B **84**, 184515 (2011).

[20] É. Dumur, B. Küng, A. K. Feofanov, T. Weissl, N. Roch, C. Naud, W. Guichard, and O. Buisson, V-shaped superconducting artificial atom based on two inductively coupled transmons, Phys. Rev. B **92**, 020515 (2015).

[21] N. Bergeal, R. Vijay, V. E. Manucharyan, I. Siddiqi, R. J. Schoelkopf, S. M. Girvin, and M. H. Devoret, Analog

information processing at the quantum limit with a Josephson ring modulator, Nat. Phys. **6**, 296 (2010).

[22] N. Bergeal, F. Schackert, M. Metcalfe, R. Vijay, V. E. Manucharyan, L. Frunzio, D. E. Prober, R. J. Schoelkopf, S. M. Girvin, and M. H. Devoret, Phase-preserving amplification near the quantum limit with a Josephson ring modulator, Nature (London) **465**, 64 (2010).

[23] Hanhee Paik, D. I. Schuster, Lev S. Bishop, G. Kirchmair, G. Catelani, A. P. Sears, B. R. Johnson, M. J. Reagor, L. Frunzio, L. I. Glazman, S. M. Girvin, M. H. Devoret, and R. J. Schoelkopf, Observation of High Coherence in Josephson Junction Qubits Measured in a Three-Dimensional Circuit QED Architecture, Phys. Rev. Lett. **107**, 240501 (2011).

[24] J. H. Plantenberg, P. C. De Groot, C. J. P. M. Harmans, and J. E. Mooij, Demonstration of controlled-NOT quantum gates on a pair of superconducting quantum bits, Nature (London) **447**, 836 (2007).

[25] P. C. De Groot, J. Lisenfeld, R. N. Schouten, S. Ashhab, A. Lupaşcu, C. J. P. M. Harmans, and J. E. Mooij, Selective darkening of degenerate transitions demonstrated with two superconducting quantum bits, Nat. Phys. **6**, 763 (2010).

[26] L. M. K. Vandersypen and I. L. Chuang, NMR techniques for quantum control and computation, Rev. Mod. Phys. **76**, 1037 (2005).

[27] M. Hatridge, R. Vijay, D. H. Slichter, John Clarke, and I. Siddiqi, Dispersive magnetometry with a quantum limited SQUID parametric amplifier, Phys. Rev. B **83**, 134501 (2011).

[28] Adriano Barenco, David Deutsch, Artur Ekert, and Richard Jozsa, Conditional Quantum Dynamics and Logic Gates, Phys. Rev. Lett. **74**, 4083 (1995).

[29] Farrokh Vatan and Colin Williams, Optimal quantum circuits for general two-qubit gates, Phys. Rev. A **69**, 032315 (2004).

[30] J. M. Chow, J. M. Gambetta, L. Tornberg, Jens Koch, Lev S. Bishop, A. A. Houck, B. R. Johnson, L. Frunzio, S. M. Girvin, and R. J. Schoelkopf, Randomized Benchmarking and Process Tomography for Gate Errors in a Solid-State Qubit, Phys. Rev. Lett. **102**, 090502 (2009).

[31] M. Dalmonte, S. I. Mirzaei, P. R. Muppalla, D. Marcos, P. Zoller, and G. Kirchmair, Realizing dipolar spin models with arrays of superconducting qubits, Phys. Rev. B **92**, 174507 (2015).

[32] Lin-Mei Liang and Cheng-Zu Li, Realization of quantum SWAP gate between flying and stationary qubits, Phys. Rev. A **72**, 024303 (2005).

[33] Raj B. Patel, Joseph Ho, Franck Ferreyrol, Timothy C. Ralph, and Geoff J. Pryde, A quantum Fredkin gate, Sci. Adv. **2**, e1501531 (2016).

[34] A. Fedorov, L. Steffen, M. Baur, M. P. da Silva, and A. Wallraff, Implementation of a Toffoli gate with superconducting circuits, Nature (London) **481**, 170 (2012).

[35] M. D. Reed, L. DiCarlo, S. E. Nigg, L. Sun, L. Frunzio, S. M. Girvin, and R. J. Schoelkopf, Realization of three-qubit quantum error correction with superconducting circuits, Nature (London) **482**, 382 (2012).

[36] K. M. Sliwa, M. Hatridge, A. Narla, S. Shankar, L. Frunzio, R. J. Schoelkopf, and M. H. Devoret, Reconfigurable

Josephson Circulator/Directional Amplifier, Phys. Rev. X **5,** 041020 (2015).

[37] D. H. Slichter, O. Naaman, and I. Siddiqi, Millikelvin thermal and electrical performance of lossy transmission line filters, Appl. Phys. Lett. **94,** 192508 (2009).

[38] Alexandre Blais, Ren-Shou Huang, Andreas Wallraff, S. M. Girvin, and R. J. Schoelkopf, Cavity quantum electrodynamics for superconducting electrical circuits: An architecture for quantum computation, Phys. Rev. A **69,** 062320 (2004).

[39] D. I. Schuster, A. Wallraff, A. Blais, L. Frunzio, R.-S. Huang, J. Majer, S. M. Girvin, and R. J. Schoelkopf, ac Stark Shift and Dephasing of a Superconducting Qubit Strongly Coupled to a Cavity Field, Phys. Rev. Lett. **94,** 123602 (2005).

[40] L. DiCarlo, J. M. Chow, J. M. Gambetta, Lev S. Bishop, B. R. Johnson, D. I. Schuster, J. Majer, A. Blais, L. Frunzio, S. M. Girvin, and R. J. Schoelkopf, Demonstration of two-qubit algorithms with a superconducting quantum processor, Nature (London) **460,** 240 (2009).

[41] S. Filipp, P. Maurer, P. J. Leek, M. Baur, R. Bianchetti, J. M. Fink, M. Göppl, L. Steffen, J. M. Gambetta, A. Blais, and A. Wallraff, Two-Qubit State Tomography Using a Joint Dispersive Readout, Phys. Rev. Lett. **102,** 200402 (2009).

[42] Daniel F. V. James, Paul G. Kwiat, William J. Munro, and Andrew G. White, Measurement of qubits, Phys. Rev. A **64,** 052312 (2001).

[43] Z. Hradil, Quantum-state estimation, Phys. Rev. A **55,** R1561 (1997).

[44] Max S. Kaznady and Daniel F. V. James, Numerical strategies for quantum tomography: Alternatives to full optimization, Phys. Rev. A **79,** 022109 (2009).